EPR and electron-nuclear-double-resonance investigations of Fe^{3+} in $KMgF_3$

D. C. Stjern and R. C. DuVarney
Physics Department, Emory University, Atlanta, Georgia 30322
W. P. Unruh
Department of Physics and Astronomy, University of Kansas, Lawrence, Kansas 66044
(Received 4 February 1974)

Single crystals of iron-doped $KMgF_3$ show a strong axial EPR spectrum with partially resolved hyperfine structure. The spectrum arises from Fe^{3+} in a crystalline field of [100] axial symmetry. An electron-nuclear-double-resonance study of the hyperfine interaction gives positive support to the model previously proposed. The iron ion substitutes for a magnesium ion, and one of the surrounding six-nearest-neighbor fluorine ions is either missing or replaced by a charge-compensating impurity such as O^{--}, thus giving rise to an axial distortion. The measured values for the spin-Hamiltonian parameters are $D = 0.352 \pm 0.005\ cm^{-1}$, $g_{\parallel} = 2.0042 \pm 0.0005$, and $g_{\perp} = 2.0120 \pm 0.0005$, where g is axially symmetric about the symmetric axis of the crystalline-field parameter D. The nearest-neighbor hyperfine interaction constants are $A_{\parallel}/h = 104.6 \pm 0.1$ MHz and $A_{\perp}/h = 55.7 \pm 0.1$ MHz for the four ^{19}F ions in a (100) plane perpendicular to the symmetry axis of D, and $A_{\parallel}/h = 43.2 \pm 0.5$ MHz, $A_{\perp}/h = 24.6 \pm 0.1$ MHz for the single ^{19}F ion along the symmetry axis of D. It is assumed that the hyperfine interaction tensors are axially symmetric about their corresponding Fe–F bond directions.

I. INTRODUCTION

Strong axial electron-paramagnetic-resonance (EPR) spectra stemming from the ferric ion (Fe^{3+}) in cubic perovskite-type materials have been reported in the literature by several authors. Previous EPR work on $BaTiO_3$,[1] $PbTiO_3$,[2] $SrTiO_3$,[3] and $KTaO_3$[4] and theoretical studies by Griffith[5] have shown that the observed paramagnetic spectra can be explained in terms of the ground-state splitting of trivalent iron ($3d^5$, $^6S_{5/2}$) produced by an axial crystalline electric field. Under the action of a tetragonal crystalline field, this ground state splits into three twofold-degenerate levels, and its behavior in the presence of a magnetic field can be described by a spin Hamiltonian containing, in addition to the electronic Zeeman term, a crystalline-field term of the second degree. In the study of iron-doped strontium titanate by Kirkpatric *et al.*,[3] accurate measurements of the EPR field positions at two different klystron frequencies (X and Ku band) allowed the determination of the crystalline-field parameter $|2D| = 2.85 \pm 0.15\ cm^{-1}$. They concluded that, with Fe^{3+} residing in a Ti^{4+} site, the only possible explanation for such a large crystalline field is that local charge compensation takes place through a nearest-neighbor oxygen vacancy. A similar conclusion had been made by Wemple[4] to explain the axial spectrum detected in samples of iron-doped potassium tantalate.

Recently, Kolopus *et al.*[6] reported a strong axial EPR spectrum in iron-doped potassium magnesium fluoride ($KMgF_3$). They tentatively interpreted the spectrum as arising from Fe^{3+} in a crystalline field of [100] axial symmetry. Nearest-neighbor (NN) ^{19}F superhyperfine (shf) structure was observed, and this suggested that Fe^{3+} is incorporated into the lattice substitutionally for Mg^{2+}. The shf patterns showed that only five of the NN fluorine ions are present, with the sixth site possibly being filled by a divalent negative ion with zero nuclear spin. A complete analysis of the spectrum was not possible because of lack of resolution in the EPR spectrum at certain angles, which led to an uncertainty in assigning the size and number of splittings to be attributed to the observed shf structure.

In this paper, we report the results of an EPR and electron-nuclear double-resonance (ENDOR) study of single crystals of iron-doped $KMgF_3$. These crystals show the strong axial EPR spectrum with shf structure previously reported.[6] The EPR and ENDOR results presented here complete the previous analysis of the spectrum and confirm the earlier interpretation. In addition, they give new values for the electronic g-tensor components, the crystalline-field parameter, and the shf-interaction parameters.

II. EXPERIMENTAL

The $KMgF_3$ single crystals that were used in this study were supplied by Abraham of Oak Ridge National Laboratory. In appearance they were transparent, colorless, and from 64 to 250 mm^3 in volume. Each of the crystals had at least one identifiable face corresponding to a (100) cleavage plane. Other principal directions were obtained by x-ray diffraction techniques.

The EPR studies were done on an X-band homodyne spectrometer equipped with 100-kHz field modulation and phase-sensitive detection. Measurements were made at 300, 77, and 20 °K employing a Varian V-4531 cavity system operating in the TE_{102} mode. The 9-in. electromagnet was field regulated, and accurate measurements of the magnetic field were made with a proton probe and frequency counter. The klystron frequency was also measured with this counter used in conjunc-

tion with a plug-in frequency converter for X band.

The ENDOR measurements were made at 4.2 °K on an X-band superheterodyne spectrometer, with the sample and cavity immersed in liquid helium. The nuclear resonance frequency was obtained from a voltage-swept oscillator slaved to a 1024-memory-address signal averager. Amplification of this low-level rf power was obtained from a broad band (0.2–220 MHz) 10-W power amplifier driving a coil wrapped around the bottom end of a rectangular TE_{102} microwave cavity which had been split along the broad wall. The sample was mounted on the bottom wall of the cavity directly on the split, where the rf field entering the cavity was most intense. The ENDOR coil was in series with terminated coaxial lines into the Dewar, and this nominal match allowed broad-band frequency sweeps without adjustment. The video output of the EPR spectrometer was averaged directly, and data were recorded from the signal-averager memory after several hundred rapid sweeps through the frequency range of interest. A sweep rate of ~ 50 MHz/sec was generally used with 10-MHz/sec sweep rate for detailed examination of a particular region of the spectrum. ENDOR responses occurred at frequencies as high as ~ 210 MHz. Spectra were accumulated in the signal averager along with standard frequency markers generated dynamically during the rapid sweep. Positions of the ENDOR lines could be measured, typically, to within 200–500 kHz, the limit set by the linewidths of the ENDOR transitions.

III. SPIN-HAMILTONIAN CALCULATIONS

The EPR and ENDOR spectra produced by the Fe^{3+} ion in an axially symmetric crystalline field are well described by the spin Hamiltonian

$$\mathcal{H} = \mu_B \vec{B}_0 \cdot \overleftrightarrow{g} \cdot \vec{S} + \vec{S} \cdot \overleftrightarrow{D} \cdot \vec{S} + \sum_\alpha [\vec{I}^\alpha \cdot \overleftrightarrow{A} \cdot \vec{S} - \gamma_n \hbar \vec{I}^\alpha \cdot \vec{B}_0] , \quad (1)$$

where the sums are over the interacting nuclei in the vicinity of the Fe^{3+} ion. For this work, only fluorine shf interactions were observed so that $I = \frac{1}{2}$ and there are no electric quadrupole terms in the Hamiltonian. We let the coordinates (x, y, z) denote the principal axis system of the D tensor and assume that the $\overleftrightarrow{D}$, $\overleftrightarrow{g}$, and $\overleftrightarrow{A}$ tensors all have the same principal axes. The z axis denotes the symmetry axis of $\overleftrightarrow{D}$, and the $\overleftrightarrow{g}$ tensor is assumed to have axial symmetry about this axis also, so that $g_{xx} = g_\perp$, $g_{yy} = g_\perp$, and $g_{zz} = g_\parallel$.

The observed angular dependence of the EPR spectra discussed below indicates that the electronic Zeeman interaction is of the same order of magnitude as D for experiments at X-band frequencies. Thus, analyses of the data using perturbation treatments of Eq. (1) are not valid, and one must, instead, resort to direct diagonalization of the appropriate spin-Hamiltonian matrix. Three types of matrices were used in the analysis of the data presented here.

The simplest matrix was used to determine $g_\parallel$ and estimate $g_\perp$ and D by fitting the predicted angular dependence of the centroid of the EPR spectrum to the data. Neglecting the hyperfine interaction terms in Eq. (1) and assuming that the external magnetic field B_0 lies in the xz plane making an angle θ with the z axis, Eq. (1) becomes

$$\mathcal{H}_c = \mu_B B_0 (g_\perp \sin\theta S_x + g_\parallel \cos\theta S_z) + D[S_z^2 - \tfrac{1}{3} S(S+1)] , \quad (2)$$

where the $\vec{S} \cdot \overleftrightarrow{D} \cdot \vec{S}$ term has been expressed in the more convenient axial form.[7] The matrix constructed from Eq. (2) is (row and column entries are in the order $|\frac{1}{2}\rangle$, $|-\frac{1}{2}\rangle$, $|\frac{3}{2}\rangle$, $|-\frac{3}{2}\rangle$)

$$\langle M_S | \mathcal{H}_c | M_S' \rangle = \begin{bmatrix} G_\parallel - 4D' & 3G_\perp & \sqrt{8}G_\perp & 0 \\ 3G_\perp & -G_\parallel - 4D' & 0 & \sqrt{8}G_\perp \\ \sqrt{8}G_\perp & 0 & 3G_\parallel - D' & 0 \\ 0 & \sqrt{8}G_\perp & 0 & -3G_\parallel - D' \end{bmatrix} , \quad (3)$$

where $G_\parallel = \frac{1}{2} g_\parallel \mu_B B_0 \cos\theta$, $G_\perp = \frac{1}{2} g_\perp \mu_B B_0 \sin\theta$, and $D' = 2D/3$. The $M_S = \pm 5/2$ states have been neglected. For EPR measurements at X-band, one is interested in transitions between the $M_S = +\frac{1}{2}$ and $-\frac{1}{2}$ levels. There are no off-diagonal elements which connect the $\pm\frac{1}{2}$ states directly to the $\pm\frac{5}{2}$ states. With D approximately equal to or larger than the electronic Zeeman interaction, the influence of the $\pm\frac{5}{2}$ states on the EPR spectra will be negligibly small.

The second type of matrix used in the analysis of the data includes terms arising from the shf interaction of the unpaired electronic spin with a single fluorine nucleus, $I = \frac{1}{2}$. The appropriate spin Hamiltonian for the description of shf structure in the EPR spectra is

$$\mathcal{H}_1 = \mathcal{H}_c + A_{xx} I_x S_x + A_{yy} I_y S_y + A_{zz} I_z S_z - \gamma_n \hbar B_0 (I_x \sin\theta + I_z \cos\theta) , \quad (4)$$

where $\mathcal{H}_c$ is defined by Eq. (2). Employing simple product states $\langle M_S, M_I |$, the matrix constructed from Eq. (4) is (row and column entries are in the order $|\frac{1}{2}\,\frac{1}{2}\rangle$, $|\frac{1}{2}\,-\frac{1}{2}\rangle$, $|-\frac{1}{2}\,\frac{1}{2}\rangle$, $|-\frac{1}{2}\,-\frac{1}{2}\rangle$, $|\frac{3}{2}\,\frac{1}{2}\rangle$, $|\frac{3}{2}\,-\frac{1}{2}\rangle$, $|-\frac{3}{2}\,\frac{1}{2}\rangle$, $|-\frac{3}{2}\,-\frac{1}{2}\rangle$)

$$\langle M_S M_1 | \mathcal{H}_1 | M_S' M \rangle =$$

$$\begin{bmatrix}
G_{\parallel}-4D'+A_{zz}/4-F_{\parallel} & -F_{\perp} & 3G_{\perp} & 3A_-/4 & \sqrt{8}G_{\perp} & \sqrt{2}A_+/2 & 0 & 0 \\
-F_{\perp} & G_{\parallel}-4D'-A_{zz}/4+F_{\parallel} & 3A_+/4 & 3G_{\perp} & \sqrt{2}A_-/2 & \sqrt{8}G_{\perp} & 0 & 0 \\
3G_{\perp} & 3A_+/4 & -G_{\parallel}-4D'-A_{zz}/4-F_{\parallel} & -F_{\perp} & 0 & 0 & \sqrt{8}G_{\perp} & \sqrt{2}A_-/2 \\
3A_-/4 & 3G_{\perp} & -F_{\perp} & -G_{\parallel}-4D'+A_{zz}/4+F_{\parallel} & 0 & 0 & \sqrt{2}A_+/2 & \sqrt{8}G_{\perp} \\
\sqrt{8}G_{\perp} & \sqrt{2}A_-/2 & 0 & 0 & 3G_{\parallel}-D'+3A_{zz}/4-F_{\parallel} & -F_{\perp} & 0 & 0 \\
\sqrt{2}A_+/2 & \sqrt{8}G_{\perp} & 0 & 0 & -F_{\perp} & 3G_{\parallel}-D'-3A_{zz}/4+F_{\parallel} & 0 & 0 \\
0 & 0 & \sqrt{8}G_{\perp} & \sqrt{2}A_+/2 & 0 & 0 & -3G_{\parallel}-D'-3A_{zz}/4-F_{\parallel} & -F_{\perp} \\
0 & 0 & \sqrt{2}A_-/2 & \sqrt{8}G_{\perp} & 0 & 0 & -F_{\perp} & -3G_{\parallel}-D'+3A_{zz}/4+F_{\parallel}
\end{bmatrix} , \quad (5)$$

where $A_+ = A_{xx}+A_{yy}$, $A_- = A_{xx}-A_{yy}$, $F_{\parallel} = \frac{1}{2}\gamma_n \hbar B_0 \cos\theta$ and $F_{\perp} = \frac{1}{2}\gamma_n \hbar B_0 \sin\theta$.

This matrix works well in predicting the observed EPR spectra, including the shf structure, but fails to predict the proper ENDOR transition frequencies at all orientations. These complications arise because of the large hyperfine interactions by magnetically equivalent fluorine nuclei. Such conditions lead to additional line splitting of the ENDOR spectrum through indirect nuclear-nuclear coupling.[8-12] The size of these splittings may be several MHz when large shf interactions (~ 100 MHz) are involved. We must therefore consider the spin Hamiltonian matrix for magnetically equivalent nuclei. The discussion may be limited to equivalent pairs having inversion symmetry through the Fe^{3+} ion. In this context it is appropriate to introduce a total-nuclear-spin operator $F = I^{(1)} + I^{(2)}$. The spin Hamiltonian is now given by

$$\mathcal{H}_2 = \mathcal{H}_c + A_{xx} S_x F_x + A_{yy} S_y F_y + A_{zz} S_z F_z - \gamma_n \hbar B_0 (F_x \sin\theta + F_z \cos\theta) , \quad (6)$$

where $\mathcal{H}_c$ is again defined by Eq. (2). The total nuclear wave functions are conveniently expressed in a representation of symmetrized product states, specified by the total nuclear quantum numbers $F = 0, 1$ and the projection quantum numbers $\{M_F\} = \{0\}, \{0, \pm 1\}$. The new wave functions $|F, M_F\rangle$ become

$$\begin{aligned}
|1, 1\rangle &= |\tfrac{1}{2}\rangle|\tfrac{1}{2}\rangle , \\
|1, 0\rangle &= \sqrt{\tfrac{1}{2}}\,(|\tfrac{1}{2}\rangle|-\tfrac{1}{2}\rangle + |-\tfrac{1}{2}\rangle|\tfrac{1}{2}\rangle) , \\
|1, -1\rangle &= |-\tfrac{1}{2}\rangle|-\tfrac{1}{2}\rangle , \quad (7)
\end{aligned}$$

and

$$|0, 0\rangle = \sqrt{\tfrac{1}{2}}\,(|\tfrac{1}{2}\rangle|-\tfrac{1}{2}\rangle - |-\tfrac{1}{2}\rangle|\tfrac{1}{2}\rangle) .$$

The electron-nuclear wave functions are then given by the product states

$$|S, M_S, F, M_F\rangle = |S, M_S\rangle |F, M_F\rangle . \quad (8)$$

Since Eq. (6) is symmetric under interchange of nuclear spins $I^{(1)}$ and $I^{(2)}$, it does not connect symmetric and antisymmetric states. Thus, we calculate the transition frequencies and degeneracy splittings in the ENDOR spectra from the matrix formed by Eq. (6) within the nuclear manifold $F = 1$. Labeling the electron-nuclear states by the M_S and M_F quantum numbers ($M_S = \pm 1/2, \pm 3/2$; $M_F = 0, \pm 1$), the spin-Hamiltonian matrix becomes (row and column order is $|\frac{1}{2}1\rangle$, $|\frac{1}{2}0\rangle$, $|\frac{1}{2}-1\rangle$, $|-\frac{1}{2}1\rangle$, $|-\frac{1}{2}0\rangle$, $|-\frac{1}{2}-1\rangle$, $|\frac{3}{2}1\rangle$, $|\frac{3}{2}0\rangle$, $|\frac{3}{2}-1\rangle$, $|-\frac{3}{2}1\rangle$, $|-\frac{3}{2}0\rangle$, $|-\frac{3}{2}-1\rangle$)

$$
\langle M_S M_F' | \mathcal{H}_2 | M_S' M_F' \rangle =
\begin{bmatrix}
G_{\parallel} - 4D' + A_{zz}/2 - 2F_{\parallel} & -\sqrt{2}F_{\perp} & 0 & 3G_{\perp} & 3A_-/\sqrt{8} & 0 & \sqrt{8}G_{\perp} & A_+ & 0 & 0 & 0 & 0 \\
-\sqrt{2}F_{\perp} & G_{\parallel} - 4D' & -\sqrt{2}F_{\perp} & 3A_+/\sqrt{8} & 3G_{\perp} & 3A_-/\sqrt{8} & A_- & \sqrt{8}G_{\perp} & A_+ & 0 & 0 & 0 \\
0 & -\sqrt{2}F_{\perp} & G_{\parallel} - 4D' - A_{zz}/2 + 2F_{\parallel} & 0 & 3A_+/\sqrt{8} & 3G_{\perp} & 0 & A_- & \sqrt{8}G_{\perp} & 0 & 0 & 0 \\
3G_{\perp} & 3A_+/\sqrt{8} & 0 & -G_{\parallel} - 4D' - A_{zz}/2 - 2F_{\parallel} & -\sqrt{2}F_{\perp} & 0 & 0 & 0 & 0 & \sqrt{8}G_{\perp} & A_- & 0 \\
3A_-/\sqrt{8} & 3G_{\perp} & 3A_+/\sqrt{8} & -\sqrt{2}F_{\perp} & -G_{\parallel} - 4D' & -\sqrt{2}F_{\perp} & 0 & 0 & 0 & A_+ & \sqrt{8}G_{\perp} & A_- \\
0 & 3A_-/\sqrt{8} & 3G_{\perp} & 0 & -\sqrt{2}F_{\perp} & -G_{\parallel} - 4D' + A_{zz}/2 + 2F_{\parallel} & 0 & 0 & 0 & A_+ & \sqrt{8}G_{\perp} & \\
\sqrt{8}G_{\perp} & A_- & 0 & 0 & 0 & 0 & 3G_{\parallel} - D' + 3A_{zz}/2 - 2F_{\parallel} & -\sqrt{2}F_{\perp} & 0 & 0 & 0 & 0 \\
A_+ & \sqrt{8}G_{\perp} & A_- & 0 & 0 & 0 & -\sqrt{2}F_{\perp} & 3G_{\parallel} - D' & -\sqrt{2}F_{\perp} & 0 & 0 & 0 \\
0 & A_+ & \sqrt{8}G_{\perp} & 0 & 0 & 0 & 0 & -\sqrt{2}F_{\perp} & 3G_{\parallel} - D' - 3A_{zz}/2 + 2F_{\parallel} & 0 & 0 & 0 \\
0 & 0 & 0 & \sqrt{8}G_{\perp} & A_+ & 0 & 0 & 0 & 0 & -3G_{\parallel} - D' - 3A_{zz}/2 - 2F_{\parallel} & -\sqrt{2}F_{\perp} & 0 \\
0 & 0 & 0 & A_- & \sqrt{8}G_{\perp} & A_+ & 0 & 0 & 0 & -\sqrt{2}F_{\perp} & -3G_{\parallel} - D' & -\sqrt{2}F_{\perp} \\
0 & 0 & 0 & 0 & A_- & \sqrt{8}G_{\perp} & 0 & 0 & 0 & 0 & -\sqrt{2}F_{\perp} & -3G_{\parallel} - D' + 3A_{zz}/2 + 2F_{\parallel}
\end{bmatrix}
, \quad (9)
$$

where $A_+ = A_{xx} + A_{yy}$, $A_- = A_{xx} - A_{yy}$, $F_\parallel = \frac{1}{2}\gamma_n \hbar B_0 \cos\theta$, and $F_\perp = \frac{1}{2}\gamma_n \hbar B_0 \sin\theta$. With Eq. (9) in diagonal form, appropriate differences of the eigenvalues can be taken to obtain ENDOR frequencies obeying the selection rules $\Delta M_F = \pm 1$, $\Delta M_S = 0$, with $M_S = +\frac{1}{2}$ and $-\frac{1}{2}$. The predicted degeneracy splittings will be compared with the observed splittings for the specific cases given below. The degeneracy splittings to be expected in the ENDOR spectrum for more than two magnetically equivalent nuclei were not worked out. Higher degeneracy (fourfold) occurs for only two angles, making such a complex calculation unnecessary for the interpretation of our results.

A computer was employed to diagonalize Eqs. (3), (5), and (9). The technique used was the Jacobi method of annihilation of off-diagonal elements.[13,14] This method provided eigenvalues which were accurate to $\pm 10^{-8}$ cm^{-1}. The accuracy of the calculations was therefore well within experimental error, in view of the EPR linewidths of ~2 G (5×10^{-4} cm^{-1}) and the ENDOR linewidths of ~0.5 MHz (1.7×10^{-5} cm^{-1}) encountered.

IV. EXPERIMENTAL RESULTS

In order to present the EPR and ENDOR results, it is useful to first consider the crystal structure of $KMgF_3$. The diamagnetic lattice of $KMgF_3$ is the ideal cubic perovskite structure, which is preserved down to very low temperatures. The structure is formed by locating K^+ ions at the corners of a cube ($a = 3.973$ Å), with an Mg^{2+} ion at the body center and F^- ions at the face-center positions.[15] The Mg^{2+} ion has six F^- nearest neighbors along $\langle 100\rangle$ directions, while the K^+ ion has twelve F^- nearest neighbors along $\langle 110\rangle$ directions. The structure is depicted in Fig. 1.

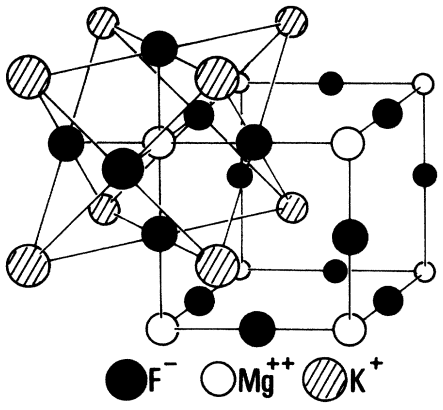

FIG. 1. Cubic perovskite crystal structure of $KMgF_3$. The Mg^{2+} ion has six F^- nearest neighbors along $\langle 100\rangle$ directions, while the K^+ ion has twelve F^- nearest neighbors along $\langle 110\rangle$ directions.

In the iron-doped samples, the Fe impurity enters substitutionally as Fe^{3+} for either magnesium or potassium. Because of size considerations, Fe^{3+} is expected to substitute for Mg^{2+} in the lattice. The symmetry properties of the superhyperfine interactions as observed by EPR and directly measured by ENDOR will clearly distinguish between the two possible impurity site locations.

The observed EPR spectrum consisted of three axially symmetric patterns with mutually perpendicular tetragonal axes. Each of the three spectra showed superhyperfine structure. Measurements were made as a function of orientation with the external magnetic field contained in a (100) plane. The angular dependence of the three spectra is plotted in Fig. 2. The dots represent the experimental points (center of each of the three spectra) and the curves are the calculated fits. Clearly, Fe^{3+} is in a strong crystalline field of [100] axial symmetry in these crystals.

Figure 3 shows the NN ^{19}F superhyperfine structure observed when the magnetic field is along a [110] direction and in a plane perpendicular to the symmetry axis of the crystalline field. The relative intensities of the ten-line pattern are 1:1:4:4:6:6:4:4:1:1, indicating that four equivalent and one inequivalent NN fluorine nuclei are involved in the interaction. From a consideration of the crystal structure given above, we can conclude that the iron ion is residing in a magnesium site. Kolopus *et al.*[6] suggested that the necessary charge compensation is provided locally, with the sixth site being filled by a divalent negative ion with zero nuclear spin. The ENDOR data presented below confirms this interpretation.

The calculated curves in Fig. 2 were obtained from a diagonalization of Eq. (3), assuming axial symmetry and common principal axes for $\overleftrightarrow{g}$ and $\overleftrightarrow{D}$. The orientation angle θ is defined by the insert in the figure. The value for $g_\parallel$ and estimates for $g_\perp$ and D were determined by fitting the data of angular variation (a) to Eq. (3), with the requirement that the energy difference between the $M_S = +\frac{1}{2}$ and $M_S = -\frac{1}{2}$ levels be equal to the klystron frequency. Although this fit is obviously highly satisfactory and gives an accurate value for $g_\parallel$, more accurate values of $g_\perp$ and D were obtained from the ENDOR measurements of the NN ^{19}F shf interactions.

The ENDOR data were analyzed using the one and two equivalent nuclei spin-Hamiltonian matrices discussed above. Relaxation effects were neglected, and the shf interaction tensors were assumed to be axially symmetric about the Fe–F bond directions. The interaction of the Fe^{3+} ion with the five NN ^{19}F nuclei could therefore be described by four shf parameters. Three of these, as well as the values for $g_\perp$ and D, were deter-

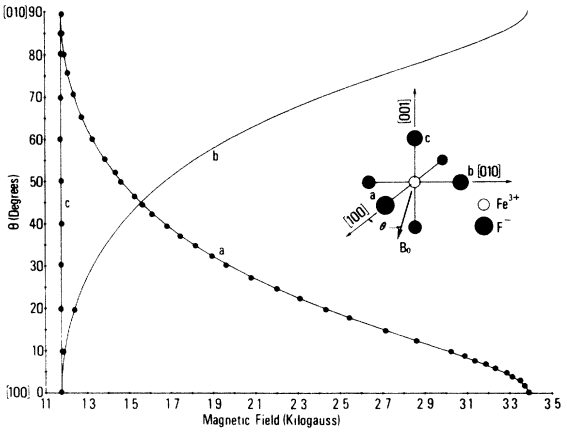

FIG. 2. Graph showing the magnetic-field positions of the centroid of the three EPR spectra vs the angle that the magnetic field makes with a [100] axis. The dots give the experimental points and the solid lines the calculated values.

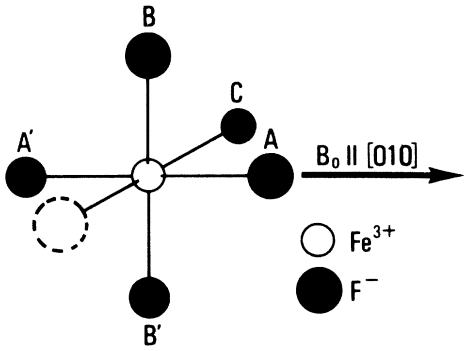

FIG. 4. Field-nuclei orientation at which the ENDOR spectrum appearing in Fig. 5 was taken. There are two equivalent pairs labeled *A-A'* and *B-B'* and one inequivalent nucleus denoted by *C*.

mined from ENDOR data taken with the magnetic field in a [010] direction, using sites for which the field direction is perpendicular to the symmetry axis of D. The geometry for this case is illustrated in Fig. 4. There are two equivalent pairs of nuclei labeled A-A' and B-B' and one inequivalent nucleus denoted by C. Survey traces of the ENDOR transitions are shown in Fig. 5, the arrows indicating the calculated line positions. Nuclear transitions within both the $M_S = +\frac{1}{2}$ and $M_S = -\frac{1}{2}$ manifolds were observed.

The field orientation for which these data were taken corresponds to setting $\theta = 90°$ in Eqs. (4) and (6). In addition, the shf parameters A_{xx}, A_{yy}, and A_{zz} were replaced by the appropriate components listed in Table I. A comparison of the observed and calculated ENDOR frequencies is given in Table II. Both the calculated frequencies and the predicted degeneracy splittings for magnetically equivalent pairs of nuclei are in good agreement with the data.

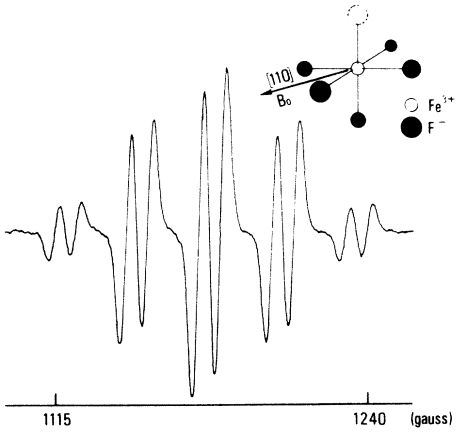

FIG. 3. EPR absorption spectrum, and the EPR spectrum showing the derivative of the absorption vs magnetic field. The magnetic field is along a [110] direction.

Values of $g_\parallel$, $g_\perp$, D, and the hyperfine coupling constants are given in Table III. $A_\parallel$ for nucleus C was obtained from the EPR spectrum with the magnetic field parallel to the principal axis of D, and its sign could not be determined. All the other signs of the shf parameters are positive relative to the positive sign of D and were obtained unambiguously from analysis of the ENDOR data. The sign of $g_\parallel$ and $g_\perp$ relative to the sign of D were determined from a consideration of the ENDOR line intensities. The higher frequency ENDOR transitions are within the $M_S = -\frac{1}{2}$ manifold. Since they are more intense than the corresponding transitions within the $M_S = +\frac{1}{2}$ manifold, as shown in Fig. 5, we assumed the $M_S = -\frac{1}{2}$ manifold to be more populated, indicating that it lies below the $M_S = +\frac{1}{2}$ manifold and, therefore, that the g – values are positive.

Figure 6(a) shows the observed EPR spectrum for the magnetic field orientation shown in Fig. 4. It consists of 14 lines with an overall width of about 120 G, whereas the expected shf structure should consist of 18 lines from two pairs of equivalent and one inequivalent nuclei. As a check on our work, we attempted to generate this spectrum

TABLE I. Assignment of the shf parameters with the appropriate parallel and perpendicular components.

Nucleus	A_{xx}	A_{yy}	A_{zz}
A, A'	$A_\parallel$	$A_\perp$	$A_\perp$
B, B'	$A_\perp$	$A_\parallel$	$A_\perp$
C	$A_\perp$	$A_\perp$	$A_\parallel$

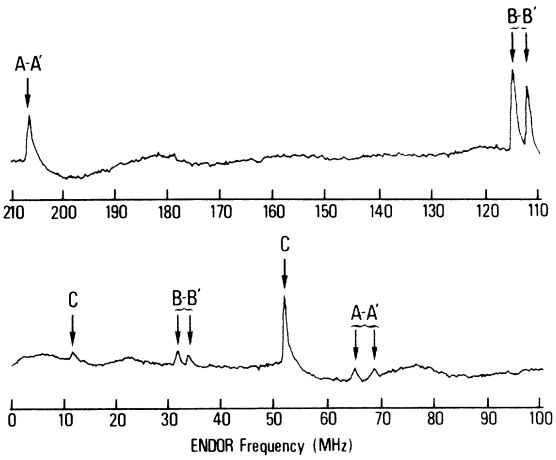

FIG. 5. Nearest-neighbor ^{19}F ENDOR spectrum. This spectrum is for the magnetic-field orientation shown in Fig. 4. Arrows show calculated ENDOR lines.

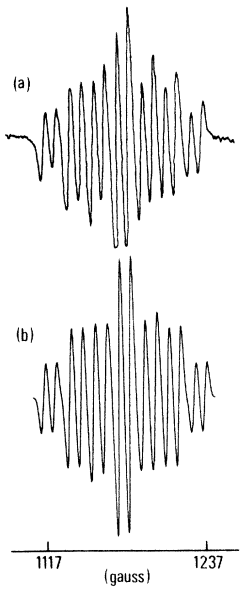

FIG. 6. Comparison of EPR spectrum with calculated pattern. (a) The EPR spectrum showing the derivative of the absorption vs magnetic field. The magnetic field orientation corresponds to the orientation shown in Fig. 4. (b) A computer-generated spectrum showing the positions of the EPR absorption lines. The pattern was constructed from the shf parameters measured by ENDOR.

on the computer using the parameters given in Table III. The result, which agrees well with the observed spectrum, is shown in Fig. 6(b).

Generating this shf structure as a function of magnetic field proved to be a noteworthy task. The difficulty occurs in converting the predicted frequency spectrum to a magnetic field spectrum, at the klystron frequency, without resorting to a five-fluorine-nuclei Hamiltonian. The usual method for generating a simulated EPR spectrum, namely, using the effective $g-$ value to convert the hyperfine interaction energies to magnetic-field splittings, gives a result that is noticeable in error here. This is because the effective $g-$ value is not constant but varies significantly over the range of magnetic field required to observe the entire spectrum. Instead, the simulation was accomplished by adjusting the magnetic field in Eq. (3) until the energy difference between the $M_S = +\frac{1}{2}$ and $M_S = -\frac{1}{2}$ eigenvalues plus and minus the net shf interaction energy due to each possible combination of NN nuclear-spin states satisfied the resonance condition. These magnetic fields then give the positions of the EPR lines. One would expect this approach to work as long as the shf interaction energies are much smaller than the energy difference between the $M_S = +\frac{1}{2}$ and $M_S = -\frac{1}{2}$ eigenvalues of Eq. (3), which is the case here.

TABLE II. Comparison of calculated and observed ENDOR frequencies for B_0 perpendicular to the symmetry axis of D and along a [010] direction.

NN ^{19}F nucleus	Calculated (MHz)	Observed (MHz)
A, A'	65.79	65.9 ± 0.1
	69.18	69.2 ± 0.1
	207.09	206.38 ± 0.1
	207.21	207.16 ± 0.1
B, B'	32.26	32.25 ± 0.1
	34.33	34.34 ± 0.1
	111.44	111.78 ± 0.1
	114.50	114.66 ± 0.1
C	12.20	12.4 ± 0.1
	52.31	52.57 ± 0.1

V. CONCLUSIONS

The results presented in Sec. IV verify that the paramagnetic complex responsible for the EPR and ENDOR spectra reported here is a trivalent iron ion residing at a magnesium site. The ENDOR results show that the shf interaction is with just five NN ^{19}F nuclei, which is the crucial evidence supporting the model. The sixth NN site may possibly be filled by a divalent negative ion

TABLE III. Spin-Hamiltonian parameters of the EPR-ENDOR spectra.

$g_\parallel = 2.0042 \pm 0.0005$		$g_\perp = 2.0120 \pm 0.0005$		$D = 0.352 \pm 0.005$ cm^{-1}
NN ^{19}F nucleus	$A_\parallel/h$ (MHz)	$A_\perp/h$ (MHz)	a/h (MHz)	b/h (MHz)
A, A'	104.6 ± 0.1	55.7 ± 0.1	72.0 ± 0.1	16.3 ± 0.06
B, B'	104.6 ± 0.1	55.7 ± 0.1	72.0 ± 0.1	16.3 ± 0.06
C	$\pm 43.2 \pm 0.5$	24.6 ± 0.1	30.8 ± 0.25	6.3 ± 0.2

TABLE IV. Fluorine shf parameters of iron-doped perovskite-type samples.

Sample	g	$A_{\parallel}/h$ (MHz)	$A_{\perp}/h$ (MHz)	a/h (MHz)	b/h (MHz)	Comments
$KCdF_3$	2.0027	102	51	68	17	a
$KZnF_3$	2.0030	106.1	52.5	70.4	17.9	b
$KMgF_3$	2.0031	108	54	72	18	c
$KMgF_3$	$g_{\parallel}=2.0042$	104.6	55.7	72.0	16.3	d
	$g_{\perp}=2.0120$	43.2	24.6	30.8	6.3	e

[a]Study of Fe^{3+}, substituting for Cd at a cubic site (see Ref. 16).

[b]Study of Fe^{3+}, substituting for Zn at a cubic site (see Ref. 17).

[c]Study of Fe^{3+}, substituting for Mg at a cubic site (see Ref. 16).

[d]shf parameters for the four NN ^{19}F ions in a plane perpendicular to the symmetry axis of D (this work).

[e]shf parameters for the single NN ^{19}F ion along the symmetry axis of D (this work).

with zero nuclear spin.

Additional evidence supporting the conclusion that the missing ^{19}F ion is replaced by a charge-compensating divalent negative ion is provided by a comparison of our results with work previously reported. Table IV lists the NN fluorine shf parameters determined in studies of other iron-doped perovskite fluorides.[16,17] Inspection of the table shows that the results of our work are consistent with the previous work, where the iron ions were in cubic crystal fields. The shf parameters for the four ^{19}F ions in a plane perpendicular to the symmetry axis of D are in good agreement, while the values for the single ^{19}F ion along the symmetry axis of D deviate considerably. If the missing fluorine site were vacant, one would expect the iron ion to be slightly displaced toward the remaining fluorine ion, with a resulting increase in the shf interaction for the single fluorine nucleus. Since the opposite is observed, our results suggest that the iron ion is slightly displaced away from the single fluorine ion, and indicate that the missing fluorine site may be filled by a divalent negative ion. The fact that no hyperfine interaction was observed for the divalent negative ion in either the EPR or ENDOR spectra leads one to conclude that it may also have zero nuclear spin. This charge-compensating ion is most likely O^{--}.

The shf interactions for the other four fluorine ions, therefore, do not have exact axial symmetry about the undistorted bond directions. However, a slight displacement of the iron ion would have much less of an effect on the shf interactions with the four planar fluorines than with the single fluorine ion that is along the axis of displacement. Any such small deviations from axial symmetry were not noticeable in our calculations of the shf parameters, and the experimental spectra were fit to within a linewidth by assuming axially symmetric shf interactions for all five NN ^{19}F nuclei.

ACKNOWLEDGMENTS

The authors wish to thank Dr. M. M. Abraham for kindly supplying the crystals used in this study. We also wish to acknowledge the many helpful discussions with Dr. Allen K. Garrison, Dr. Rodney H. Thorland, and Dr. J. W. Culvahouse. The ENDOR experiments were done at Ohio University, Athens, Ohio.

[1]A. W. Hornig, R. C. Rempel, and H. E. Weaver, J. Phys. Chem. Solids 10, 1 (1959).
[2]D. J. A. Gainon, Phys. Rev. 134, A1300 (1964).
[3]E. S. Kirkpatrick, K. A. Muller, and R. S. Rubins, Phys. Rev. 135, A86 (1964).
[4]S. Wemple, Ph. D. thesis (MIT, 1963) (unpublished).
[5]J. S. Griffith, *The Theory of Transition-Metal Ions* (Cambridge U.P., Cambridge, England, 1961), Chap. 12.
[6]J. L. Kolopus, J. T. Lewis, and W. P. Unruh, Bull. Am. Phys. Soc. 15, 248 (1970).
[7]A. Abragam and B. Bleaney, *Electron Paramagnetic Resonance of Transition Ions* (Clarendon, Oxford, 1970), p. 152.
[8]T. E. Feuchtwang, Phys. Rev. 126, 1616 (1962).
[9]J. M. Baker and J. P. Hurrell, Proc. Phys. Soc. Lond. 82, 742 (1963).
[10]R. Gazzinelli and R. L. Mieher, Phys. Rev. 175, 395 (1968).
[11]W. P. Unruh, L. G. Nelson, J. T. Lewis, and J. L. Kolopus, J. Phys. C 4, 2992 (1971).
[12]N. F. Ramsey, Phys. Rev. 91, 303 (1953).
[13]P. A. White, J. Soc. Ind. Appl. Math. 6, 393 (1958).
[14]M. Marcus, U. S. Natl. Bur. Stand. Applied Mathematics Series 57, 19 (U.S. GPO, Washington, D.C., 1964).
[15]R. W. G. Wyckoff, *Crystal Structures* (Wiley, New York, 1964), Vol. II, p. 390.
[16]T. P. P. Hall, W. Hays, R. W. H. Stevenson, and J. Wilkins, J. Chem. Phys. 38, 1977 (1963).
[17]R. K. Jeck and J. J. Krebs, Phys. Rev. B 5, 1677 (1972).